International Journal of Multiphase Flow 176 (2024) 104843

Contents lists available at ScienceDirect

International Journal of Multiphase Flow

journal homepage: www.elsevier.com/locate/ijmulflow

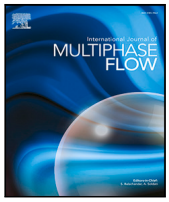

Multiphysics simulation of two-phase viscous fluid flow steered by electric field for jetting of microdroplets

Yiming Liu [a], Bilen Emek Abali [b,*], Wolfgang H. Müller [a]

[a] Technische Universität Berlin, Institute of Mechanics, Einsteinufer 5, 10587 Berlin, Germany
[b] Uppsala University, Division of Applied Mechanics, Department of Materials Science and Engineering, Box 35, SE 751 03, Uppsala, Sweden

ARTICLE INFO

Dataset link: https://github.com/liuyiming0507/FluidwithElectricField

Keywords:
Electrodynamics
Two-phase flow
Level set method
Finite element method
FEniCS

ABSTRACT

In this research, we delve into the intricacies of viscous fluid flow with electric field coupling by employing the Finite Element Method (FEM) in tandem with the level set method. We generate a weak form for satisfying governing equations for electric field and fluid velocity while two phases are tracked by the level set function. The primary focus of this study is the complex interactions between free-falling jet and electric field, and the behavior of droplet encompassing deformation, fission, and fusion under the influence of electric field. The main contribution of this paper is given a new implement by using the P1/P1 scheme to directly solve the weak forms of coupled governing equations, which significantly improves calculation efficiency compared to the P2/P1 scheme, and we open source the code. This implement is verified by comparing with the experimental results of oil droplets deforming under an electric field. Computations are performed by FEniCS open-source packages. The phenomena documented underscore the multifaceted relationship between electrodynamic forces and fluid mechanics, accentuated distinctly under non-uniform electric field conditions.

1. Introduction

For two immiscible non-conductive fluids with different electric permittivities, electric field exerts influence at their interface due to the polarization and affect the motion of the fluids. Such a complex interaction between electric polarization and fluid flow allow influencing the trajectory of the jet stream as well as the fission and fusion of droplets. Investigating the mechanisms of this issue and simulating it through appropriate numerical methods have certain applications in microfluidic control. For instance, microdroplets have numerous applications in therapeutic agent delivery, imaging processes, biomolecular synthesis, diagnostic chips, and drug delivery (Sohrabi et al., 2020; Campanholi et al., 2022; Jia and Chandru, 2023; Bowman and Alper, 2020; Wang et al., 2019; Zhai et al., 2023; Giannitelli et al., 2022). The electric field may be applied to process and control the microdroplets generation, fission and fusion (Li et al., 2023; Zagnoni et al., 2010; Chaudhuri et al., 2017). Beyond that, this multiphysics case may also be applid in electrohydrodynamic atomization (EHDA) (Wang et al., 2021a; Mehta et al., 2017), 3-D printing of piezoelectric materials (Lee and Tarbutton, 2014; Fan et al., 2022; Chen et al., 2017), and ink-jet printing (Calvert, 2001; Jeong et al., 2021).

The simulation of fluid behavior has evolved significantly since the formalization of the Navier–Stokes equations, which provided a fundamental framework for understanding viscous fluid flow (Worster et al., 2000). Computational Fluid Dynamics (CFD) then emerged as a potent tool, allowing for the modeling of intricate fluid phenomena such as turbulence and the dynamics of multi-phase flows (Ferziger et al., 2019). The Finite Element Method (FEM) and the Finite Volume Method (FVM) are both prevalent numerical techniques for addressing fluid dynamics issues. Commercial software platforms commonly employ FVM, which is known for its robustness and stability, with ongoing advancements in recent times as evidenced by Martínez-Ferrer et al. (2018), Cardiff and Demirdžić (2021), Liu et al. (2021) and Wang et al. (2013). On the other hand, FEM, characterized by its accurate results and consistent convergence characteristics for error estimation, is primarily utilized in the domain of solid mechanics. It thus seamlessly lends itself to fluid mechanics problems, particularly when considering fluid–structure interactions. Lately, its application has expanded in the fluid mechanics research realm (Hansen et al., 2019; Palzhanov et al., 2021; Hashemi et al., 2020). For instance, using standard form functions, FEM has showcased its prowess in thermodynamics and electromagnetism, demonstrating its capability in handling complex coupled cases (Abali, 2017; Abali and Reich, 2020).

Research on multi-phase flow spans a vast spectrum. We narrow its focus to an immiscible two-phase flow characterized by the dynamic interface. A primary hurdle is the precise tracking of the interfacial boundary between the phases to ensure solution accuracy. This

* Corresponding author.
E-mail address: bilenemek@abali.org (B.E. Abali).

https://doi.org/10.1016/j.ijmultiphaseflow.2024.104843
Received 7 January 2024; Received in revised form 21 March 2024; Accepted 18 April 2024
Available online 20 April 2024

boundary is characterized by a parameter called surface tension, conventionally studied in hydrostatics but applied in fluid dynamics. This underscores the necessity of computational strategies to comprehend the influence of surface tension on fluid motion more effectively. Several methodologies, like the Volume Of Fluid (VOF) method (Noh and Woodward, 1976; Sethian, 1999), the level set (LS) method (Osher et al., 2004; Scardovelli and Zaleski, 1999; Yu et al., 2023), the front tracking approach (Unverdi and Tryggvason, 1992), phase-field techniques (Villanueva and Amberg, 2006), and smoothed particle hydrodynamics (SPH) (Fernández-Gutiérrez and Zohdi, 2020; Park and Zohdi, 2020; Zhang et al., 2022; Liu et al., 2023) have been employed to model incompressible flow of immiscible two-phase fluid via the surface tension. The Level Set function provides a smooth representation of interfaces, which can enhance the accuracy of calculations for interface curvature and normal vectors, particularly important for flow problems requiring precise surface tension calculations. The smooth interface also naturally facilitates the handling of interface merging and breaking, making it especially useful in simulating flows involving complex interface dynamics, such as droplet collisions, breakups, or coalescence. However, compared to the VOF method (sharp interface), the LS method has poor mass conservation. For the scope of this paper, we follow the conservative level set (CLS) method proposed by Olsson and Kreiss (Olsson and Kreiss, 2005; Olsson et al., 2007), which addresses the mass conservation issue inherent to the LS method.

The intersection of two-phase flow with electric field is a multiphysics problem that presents unique challenges and opportunities (Ling et al., 2019; Wang et al., 2021b; Kamali and Manshadi, 2016; Ristenpart et al., 2009). In 2011, J.M. López-Herrera and S. Popinet et al. (López-Herrera, 2011) proposed a charge conservation scheme, employing the FVM and VOF method to address the two-phase electrohydrodynamics (EHD) problems. VOF method goes back to Hirt and Nichols (Hirt and Nichols, 1981). In Yang et al. (2013), Q. Yang et al. introduced a 3D phase field model for studying electrohydrodynamic two-phase flows. The research underscores the model's efficiency and capability to capture complex 3D behaviors and fluid dynamics in electrically influenced environments. In 2014, Tian et al. (2014) tackled the simulation of polymer rheology in electrically induced micro-/nanostructuring processes using EHD and the conservative level set (CLS) method. Their approach, which analyzes the dynamics based on various forces including thermodynamic instability and electrostatic forces, offers a new way to understand the full-cycle evolution of polymer structuring in EHD. Xu et al. (2020) developed a simulation method for electrohydrodynamics (EHD) incorporating a level-set-based immersed interface method (IIM) for capturing interfaces with topological changes and solving the Poisson equation for electric potential with interface jump conditions. Their simulations on drop deformation, breakup, and coalescence in both 2D and 3D contexts validate the method's effectiveness. In 2022, by employing the FVM and VOF methods, Y. Tian and H. wang et al. (Tian et al., 2022) investigated the impact of droplets on superhydrophobic substrates in an electric field. M. Ashour and N. Valizadeh et al. (Ashour et al., 2021, 2023) studied the fluid dynamics of vesicle doublet suspended in an external viscous flow using isogeometric analysis and the phase-field method, without considering the coupling of multiphysical fields. Firouznia et al. (2023) introduced a spectral boundary integral method to simulate droplet electrohydrodynamics in a uniform electric field, focusing on the nonlinear coupling of interfacial charge transport and fluid flow. By incorporating a comprehensive charge transport model and addressing numerical challenges like ringing artifacts, their method allows for a detailed analysis of significant droplet deformation. M. Shen and Ben Q. Li et al. (Shen et al., 2023) present a comprehensive 3D diffuse interface model, leveraging the Cahn-Hilliard equation coupled with Navier–Stokes equations, to examine the impact dynamics of a dielectric droplet under a horizontal electric field. It showcases how electric forces can stretch the droplet in the field direction, potentially reducing splashing by altering the lamella's rising angle against the substrate. Narváez-Muñoz et al. (2023) introduce a numerical model for simulating two-phase electrohydrodynamic (EHD) phenomena, which innovates by employing a combination of the enriched finite element method and level-set approaches. It excels in accurately capturing discontinuities in fluid pressure and electric potential gradients, crucial for modeling complex EHD problems such as droplet deformation in 3D scenarios. Among the above-mentioned studies, many works combine the finite element method with LS or CLS. However, it should be pointed out that LS (also CLS) is a smooth interface method. The finer the mesh, the more accurate the interface simulation. Finer mesh often means higher computing resource requirements. In order to improve the computational efficiency and accuracy of interface simulation, some methods such as adaptive mesh refinement (AMR) have been combined with the CLS method (Antepara et al., 2021).

In this work, we propose another way to improve efficiency, by utilizing the P1/P1 scheme to directly solve the weak forms of coupled governing equations. This significantly improved computational efficiency, permitting the use of finer meshes for more detailed simulation of the interface and we open-sourced the code of this work. We verify it by comparing our numerical results with the experimental results of oil droplets deforming under an electric field from Rickert (2023). It should be pointed out that we do not use the AMR method and the method in this work has the potential to be combined with AMR to further improve computational efficiency. Besides, by integrating Gauß's law for electrodynamics with the CLS method, we introduce a novel weak form, used to mitigate convergence issues associated with the inclusion of the level set function. Drawing on the example of a free-falling jet, we showcase the interplay between the electric fields (both uniform and non-uniform electric fields) and fluid dynamics. Furthermore, we delve into the deformation and breakup behaviors of microdroplets under the influence of an electric field. The numerical simulation is carried out using the open-source packages developed by the FEniCS platform.[1] All codes are made public on Github[2] and available for use under GNU Public license (GNU Operating System, 2007).

2. Numerical methods

2.1. Two-phase flow

Balance of mass and momentum reads the continuity and momentum equations for an incompressible flow, as follows (based on the one-fluid formulation):

$$\nabla \cdot \boldsymbol{v} = 0 \tag{1}$$

and

$$\rho \frac{\partial \boldsymbol{v}}{\partial t} + \rho(\boldsymbol{v} \cdot \nabla)\boldsymbol{v} = \nabla \cdot \boldsymbol{\sigma} + \boldsymbol{f}, \tag{2}$$

respectively, where the Cauchy stress tensor, $\boldsymbol{\sigma}$, as well as volumetric force density, $\boldsymbol{f}$, need to be defined. For the stress tensor, we use the well-known linear material model, $\boldsymbol{\sigma} = -p\mathbf{I} + \mu(\nabla \boldsymbol{v} + (\nabla \boldsymbol{v})^{\intercal})$. As volumetric force densities, we decompose this term into three terms:

- body force density, $\boldsymbol{f}_g = \rho g \boldsymbol{e}_g$, due to the gravitational specific force with the known magnitude $g = 9.81\,\mathrm{N/kg}$,
- force density, $\boldsymbol{f}_s$, due to surface tension that is discussed in the following,
- and the Lorentz force density, $\boldsymbol{f}_{\mathrm{el}}$, as an electromotive effect defined in the following.

[1] The FEniCS computing platform, https://fenicsproject.org/

[2] Yiming Liu's Github account, https://github.com/liuyiming0507/FluidwithElectricField

Consequently, in order to capture the progression of the interface, thus track the two phases, one resolves the balance of mass as an advection equation, following the CLS method (Olsson and Kreiss, 2005; Olsson et al., 2007):

$$\frac{\partial \phi_c}{\partial t} + \boldsymbol{\nabla} \cdot (\phi_c \boldsymbol{v}) = 0. \tag{3}$$

This order function is a sigmoid function changing from 0 to 1 along the so-called interface. The minimum and maximum values 0 and 1 represent phases 1 and 2. For an initial condition, with the known interface between phases, we use the position of the interface, $\boldsymbol{x}_{\text{int}}$, in order to define a so-called signed distance function:

$$\phi_d(\boldsymbol{x}) = \begin{cases} \min\limits_{\boldsymbol{x}_{\text{int}} \in \Gamma} \left| \boldsymbol{x} - \boldsymbol{x}_{\text{int}} \right|, & \boldsymbol{x} \in \Omega_1, \\ -\min\limits_{\boldsymbol{x}_{\text{int}} \in \Gamma} \left| \boldsymbol{x} - \boldsymbol{x}_{\text{int}} \right|, & \boldsymbol{x} \in \Omega_2, \end{cases} \tag{4}$$

where Ω_1 and Ω_2 are subdomains that represent two different phases separated by an interface, $\Gamma = \Omega_1 \bigcap \Omega_2$. With this initially given distance function, we approximate the characteristic level set function, ϕ_c, by a sigmoid function,

$$\phi_c(\boldsymbol{x}) = \frac{1}{1 + \exp\left(\phi_d(\boldsymbol{x})/\varepsilon\right)}. \tag{5}$$

Then the solution of advection function determines the level set function. In order to ensure that the characteristic level set function, ϕ_c, maintains a continuous function at the interface at each solution time step. Reinitialization need to be used in this method. According to the CLS method, we choose the following equation as the governing equation for reinitialization:

$$\frac{\partial \phi_r}{\partial \tau} + \boldsymbol{\nabla} \cdot \left[\phi_r \left(1 - \phi_r\right) \mathbf{n}_\Gamma \left(\boldsymbol{x}, t_i\right)\right] = \varepsilon \boldsymbol{\nabla} \cdot \left[\mathbf{n}_\Gamma \left(\boldsymbol{x}, t_i\right) \left(\boldsymbol{\nabla} \phi_r \cdot \mathbf{n}_\Gamma \left(\boldsymbol{x}, t_i\right)\right)\right], \tag{6}$$

where $\mathbf{n}_\Gamma \left(\boldsymbol{x}, t_i\right)$ is the surface normal on the interface with a thickness parameter, ε, as used in Eq. (5). The divergence term (second term on the left-hand side) of Eq. (6), $\phi_r \left(1 - \phi_r\right) \mathbf{n}_\Gamma \left(\boldsymbol{x}, t_i\right)$, corresponds to the compressive flux. This artificial compression flux acts in regions where $0 < \phi_r < 1$ and in the normal direction of the interface. On the right-hand side of Eq. (6), a small amount of artificial viscosity term is introduced to avoid numerical issues caused by discontinuities at the interface. $\mathbf{n}_\Gamma \left(\boldsymbol{x}, t_i\right)$ is given by

$$\mathbf{n}_\Gamma = \frac{\boldsymbol{\nabla} \phi_c(\boldsymbol{x}, t)}{|\boldsymbol{\nabla} \phi_c(\boldsymbol{x}, t)|}. \tag{7}$$

At the time step $t = t_i$ and the initial sub-time step $\tau = 0$,

$$\phi_r(\boldsymbol{x}, 0) = \phi_c \left(\boldsymbol{x}, t_i\right). \tag{8}$$

Since the interface is tracked using ϕ_c that is a solution of the differential equation, material parameters may easily have necessary regularity conditions. In other words, there is no jump across the interface such that the material parameters in Eq. (2) may be modeled simply a mixture rule,

$$\begin{aligned} \rho &= \rho_{\text{phase1}} \phi_c + \rho_{\text{phase2}} \left(1 - \phi_c\right), \\ \mu &= \mu_{\text{phase1}} \phi_c + \mu_{\text{phase2}} \left(1 - \phi_c\right). \end{aligned} \tag{9}$$

Analogously, we use a surface tension model as in Brackbill et al. (1992), Sussman et al. (1994) by using a surface tension coefficient, σ_s, acting along the curvature of the interface, κ, as follows:

$$\boldsymbol{f}_s = \sigma_s \kappa \mathbf{n}_\Gamma \delta, \tag{10}$$

where $\mathbf{n}_\Gamma$ is the unit surface normal on the interface given by Eq. (7) and δ represents an approximation of the Dirac distribution, which is situated at the interface denoted by Γ. These are geometrically given by

$$\kappa = -\boldsymbol{\nabla} \cdot \mathbf{n}_\Gamma = -\boldsymbol{\nabla} \cdot \frac{\boldsymbol{\nabla} \phi_c}{|\boldsymbol{\nabla} \phi_c|} \tag{11}$$

and

$$\delta = \left|\boldsymbol{\nabla} \phi_c\right|. \tag{12}$$

By inserting the latter, Eq. (10) becomes

$$\boldsymbol{f}_s = \sigma_s \kappa \boldsymbol{\nabla} \phi_c. \tag{13}$$

Alternatively, we may express the surface tension force as the divergence of a surface stress tensor in an analogous manner to the bulk properties (Lafaurie et al., 1994), as follows:

$$\begin{aligned} \mathbf{T}_s &= \sigma_s \left(\mathbf{I} - \mathbf{n}_\Gamma \otimes \mathbf{n}_\Gamma\right) \delta, \\ \boldsymbol{f}_s &= \boldsymbol{\nabla} \cdot \mathbf{T}_s, \end{aligned} \tag{14}$$

where δ is given in Eq. (12). An advantage with Eq. (14) over Eq. (13) is the absence of curvature computation.

For $\boldsymbol{f}_{\text{el}}$, the interaction of electromagnetism and matter is necessary to model. Especially in a polarized medium, the choice of an accurate model is under debate (Reich et al., 2018; Abali and Queiruga, 2019; Müller and Müller; Rickert, 2023). We choose the so-called generalized Lorentz force model to represent the body force,

$$\boldsymbol{f}_{\text{el}} = \boldsymbol{\nabla} \cdot \boldsymbol{\sigma}_{\text{el}}, \tag{15}$$

under the assumption that magnetism is negligible, the electrostatic Maxwell stress tensor based on the generalized Lorentz force model, $\boldsymbol{\sigma}_{\text{el}}$, reads

$$\boldsymbol{\sigma}_{\text{el}} = \varepsilon_0 \left(\boldsymbol{E} \otimes \boldsymbol{E} - \frac{1}{2} (\boldsymbol{E} \cdot \boldsymbol{E}) \boldsymbol{I}\right). \tag{16}$$

All governing equations are formulated as a dimensionless form in order to have them in the same unit. We use the following conversion with characteristic length and time-scales in order to acquire dimensionless quantities,

$$\bar{\boldsymbol{x}} = \frac{\boldsymbol{x}}{x_0}, \bar{\boldsymbol{v}} = \frac{\boldsymbol{v}}{v_0}, \bar{t} = \frac{t}{x_0/v_0}, \bar{\rho} = \frac{\rho}{\rho_0}, \bar{\mu} = \frac{\mu}{\mu_0}, \bar{\varphi} = \frac{\varphi}{\varphi_0}, \bar{\boldsymbol{E}} = -\boldsymbol{\nabla} \bar{\varphi}, E_0 = \frac{\varphi_0}{d_0}. \tag{17}$$

Hence, we obtain the dimensionless form of Eqs. (1) and (2) as follows:

$$\boldsymbol{\nabla} \cdot \boldsymbol{v} = 0, \tag{18}$$

$$\bar{\rho} \frac{\partial \bar{\boldsymbol{v}}}{\partial \bar{t}} + \bar{\rho} (\bar{\boldsymbol{v}} \cdot \boldsymbol{\nabla}) \bar{\boldsymbol{v}} = -\boldsymbol{\nabla} \bar{p} + \frac{\bar{\mu}}{Re} \boldsymbol{\nabla} \cdot \left(\boldsymbol{\nabla} \bar{\boldsymbol{v}} + (\boldsymbol{\nabla} \bar{\boldsymbol{v}})^{\mathsf{T}}\right) + \frac{\bar{\rho}}{Fr^2} \boldsymbol{e}_g + \frac{1}{We} \bar{\boldsymbol{f}}_s + \frac{1}{El} \bar{\boldsymbol{f}}_{\text{el}}, \tag{19}$$

where Reynolds number, Re, Weber number, We, Froude number, Fr, and Electric Reynolds number El read

$$Re = \frac{\rho_0 v_0 x_0}{\mu_0}, \; Fr = \frac{v_0}{\sqrt{x_0 g}}, \; We = \frac{\rho_0 v_0^2 x_0}{\sigma_s}, \; El = \frac{\rho_0 u_0^2}{\varepsilon_0 E_0^2}. \tag{20}$$

For the computational implementation, we apply the finite difference method, also known as Euler-backward approach, to time discretization,

$$\frac{\partial \bar{\boldsymbol{v}}}{\partial \bar{t}} \approx \frac{\bar{\boldsymbol{v}} - \bar{\boldsymbol{v}}_0}{\Delta \bar{t}}. \tag{21}$$

By following a standard variational formulation, for the unknowns velocity and pressure with their variations, $\delta \bar{\boldsymbol{v}}$ and $\delta \bar{p}$, and performing partial integration on the surface tension and Lorentz force part, we obtain the weak forms:

$$F_1 = \int_\Omega \boldsymbol{\nabla} \cdot \bar{\boldsymbol{v}} \delta \bar{p} \mathrm{d}x. \tag{22}$$

$$\begin{aligned} F_2 = & \frac{1}{\Delta \bar{t}} \int_\Omega \bar{\rho} \left(\bar{\boldsymbol{v}} - \bar{\boldsymbol{v}}_0\right) \cdot \delta \bar{\boldsymbol{v}} \mathrm{d}x + \int_\Omega \bar{\rho} (\bar{\boldsymbol{v}} \cdot \boldsymbol{\nabla}) \bar{\boldsymbol{v}} \cdot \delta \bar{\boldsymbol{v}} \mathrm{d}\boldsymbol{x} - \int_\Omega \bar{p} \boldsymbol{\nabla} \cdot \delta \bar{\boldsymbol{v}} \mathrm{d}x \\ & + \frac{1}{Re} \int_\Omega \bar{\mu} \boldsymbol{\nabla} \delta \bar{\boldsymbol{v}} \cdot \left(\boldsymbol{\nabla} \bar{\boldsymbol{v}} + (\boldsymbol{\nabla} \bar{\boldsymbol{v}})^{\mathrm{T}}\right) \mathrm{d}x - \int_\Omega \delta \bar{\boldsymbol{v}} \cdot \frac{\bar{\rho}}{Fr^2} \boldsymbol{e}_g \mathrm{d}x \\ & + \int_\Omega \frac{1}{We} \mathbf{T}_s \cdot \boldsymbol{\nabla} \delta \bar{\boldsymbol{v}} + \int_\Omega \frac{1}{El} \boldsymbol{\sigma}_{\text{el}} \cdot \boldsymbol{\nabla} \delta \bar{\boldsymbol{v}} \mathrm{d}x. \end{aligned} \tag{23}$$

We selectively apply integration by parts to relevant terms only. We use the Finite Element Method (FEM) for space discretization, although

accurate, numerical instabilities may occur if Ladyzhenskaya–Babuska–Brezzi condition is not satisfied. Utilizing Taylor–Hood (P2/P1) or MINI elements for velocity and pressure is some of possible methods (John et al., 2016), yet it is computationally demanding. Particularly, when fine meshes are employed due to the interface, our aim shifts toward adopting a P1/P1 scheme. In this regard, we refer to the method introduced by Abali (2019) with an experimental validation in Abali and Savaş (2020) and tackle an additional weak form derived from the balance of angular momentum. This form is tested by $\boldsymbol{\nabla}\delta\bar{p}$ to circumvent numerical instability. Thus, we add

$$F_3 = \int_\Omega \Bigg(\left(\bar{\boldsymbol{v}} - \bar{\boldsymbol{v}}_0\right) + \Delta\bar{t}(\bar{\boldsymbol{v}}\cdot\boldsymbol{\nabla})\bar{\boldsymbol{v}} - \frac{\Delta\bar{t}}{Fr^2}\boldsymbol{e}_g - \frac{\Delta\bar{t}}{\bar{\rho}We}\boldsymbol{f}_\mathrm{s} - \frac{\Delta\bar{t}}{\bar{\rho}El}\bar{\boldsymbol{f}}_\mathrm{el} + \frac{\Delta\bar{t}}{\bar{\rho}}\boldsymbol{\nabla}\bar{p} - \frac{\Delta\bar{t}\bar{\mu}}{\bar{\rho}Re}\boldsymbol{\nabla}\cdot\left(\boldsymbol{\nabla}\bar{\boldsymbol{v}} + (\boldsymbol{\nabla}\bar{\boldsymbol{v}})^\mathrm{T}\right)\Bigg) \cdot \boldsymbol{\nabla}\delta\bar{p}\mathrm{d}x. \tag{24}$$

It should be pointed out that due to the use of P1/P1 element, $\boldsymbol{\nabla}\cdot\left(\boldsymbol{\nabla}\bar{\boldsymbol{v}} + (\boldsymbol{\nabla}\bar{\boldsymbol{v}})^\mathrm{T}\right)$ in Eq. (24) is 0, which does not influence numerical stability.

In order to track the interface between fluid and air, we use the advection and reinitialization with their normalized weak forms, respectively,

$$F_{\phi_c} = \int_\Omega \delta\phi_c \frac{\phi_c - \phi_{c0}}{\Delta\bar{t}}\mathrm{d}x - \int_\Omega \boldsymbol{\nabla}\delta\phi_c\cdot(\phi_c\bar{\boldsymbol{v}})\mathrm{d}x \tag{25}$$

$$F_{\phi_r} = \int_\Omega \delta\phi_c \frac{\phi_r - \phi_{r0}}{\Delta\bar{\tau}}\mathrm{d}x - \int_\Omega \Big(\phi_r\left(1-\phi_r\right)\left(\boldsymbol{\nabla}\delta\phi_c\cdot\mathbf{n}_\Gamma\right) + \varepsilon\left(\mathbf{n}_\Gamma\cdot\boldsymbol{\nabla}\phi_r\right)\left(\mathbf{n}_\Gamma\cdot\boldsymbol{\nabla}\delta\phi_c\right)\Big)\mathrm{d}x. \tag{26}$$

2.2. Gauß's law

From the balance of electric charge, with the charge (volume) density, q in C/m^3 (coulomb per volume), we obtain the following Maxwell equations:

$$\boldsymbol{\nabla}\cdot\boldsymbol{D} = q,\ \boldsymbol{\nabla}\times\boldsymbol{H} = \boldsymbol{J} + \varepsilon_0\frac{\partial\boldsymbol{E}}{\partial t}, \tag{27}$$

where the charge potential, $\boldsymbol{D}$ in C/m^2, current potential, $\boldsymbol{H}$ in A/m (ampere per meter), and electric current (area) density, $\boldsymbol{J}$ in A/m^2, need to be defined by constitutive equations. We use the Maxwell–Lorentz aether relations:

$$\boldsymbol{D} = \varepsilon_0\boldsymbol{E},\ \boldsymbol{H} = \frac{1}{\mu_0}\boldsymbol{B}, \tag{28}$$

where $\varepsilon_0 = 8.85\times10^{-12}\,\mathrm{A\,s/(V\,m)}$ and $\mu_0 = 4\pi\times10^{-7}\,\mathrm{V\,s/(A\,m)}$ are universal constants. We do not consider magnetism and the magnetic flux (area) density $\boldsymbol{B}$ vanishes. The total charge is composed of free and bound charges, where the free charge potential, $\mathfrak{D}$, and bound charge potential, $\boldsymbol{P}$, are introduced, as follows:

$$\boldsymbol{D} = \mathfrak{D} - \boldsymbol{P}, \tag{29}$$

where $\boldsymbol{P}$ is also known as electric polarization. For a linear material, we use

$$\mathfrak{D} = \varepsilon_0\varepsilon^\mathrm{r}\boldsymbol{E}, \tag{30}$$

where relative permittivity, ε^r, is a material parameter. Therefore, from Eq. (27), we obtain

$$\boldsymbol{\nabla}\cdot\mathfrak{D} = q^\mathrm{f}. \tag{31}$$

In this study, the different fluid parts of the two-phase flow are treated as insulators and within the system, no free charges exist. In other words, the charge potential is instantaneous and has to satisfies

$$\boldsymbol{\nabla}\cdot\mathfrak{D} = 0. \tag{32}$$

By inserting Eq. (17) and normalizing the latter, we generate the dimensionless weak form

$$\int_\Omega \boldsymbol{\nabla}\cdot\bar{\mathfrak{D}}\delta\varphi\mathrm{d}x = 0. \tag{33}$$

Similarly, we use ϕ_c to represent the relative permittivity ε^r,

$$\varepsilon^\mathrm{r} = \varepsilon^\mathrm{r}_\mathrm{phase1}\,\phi_c + \varepsilon^\mathrm{r}_\mathrm{phase2}\left(1-\phi_c\right), \tag{34}$$

where ε^r is no longer a constant, but a scalar field variable related to ϕ_c. When we put Eq. (34) into Eq. (33) there is a partial derivative calculation on ε^r. In order to avoid this item from affecting the numerical stability, we expand the equation,

$$\int_\Omega \boldsymbol{\nabla}\cdot\bar{\mathfrak{D}}\delta\varphi\mathrm{d}x = \int_\Omega \boldsymbol{\nabla}\cdot\left(\varepsilon^\mathrm{r}\boldsymbol{\nabla}\bar{\varphi}\right)\delta\varphi\mathrm{d}x = \int_\Omega\left(\varepsilon^\mathrm{r}\Delta\bar{\varphi}\delta\varphi + \left(\boldsymbol{\nabla}\varepsilon^\mathrm{r}\right)\cdot\boldsymbol{\nabla}\bar{\varphi}\delta\varphi\right)\mathrm{d}x = 0. \tag{35}$$

We divide by ε^r and use the chain rule $\boldsymbol{\nabla}\varepsilon^\mathrm{r} = \partial\varepsilon^\mathrm{r}/\partial\phi_c\boldsymbol{\nabla}\phi_c$ with Eq. (7). Then we choose to weaken the continuity condition by integrating by parts and applying Gauß's theorem and substitute Eq. (34) in it. Finally, we obtain the new weak form:

$$F_4 = \int_{\partial\Omega}\delta\varphi\boldsymbol{\nabla}\bar{\varphi}\cdot\mathbf{n}\mathrm{d}s - \int_\Omega \boldsymbol{\nabla}\bar{\varphi}\cdot\boldsymbol{\nabla}\delta\varphi\mathrm{d}x + \int_\Omega \frac{1}{\varepsilon^\mathrm{r}}\left(\varepsilon^\mathrm{r}_\mathrm{phase1} - \varepsilon^\mathrm{r}_\mathrm{phase2}\right)\left|\boldsymbol{\nabla}\phi_c\right|\mathbf{n}_\Gamma\cdot\boldsymbol{\nabla}\bar{\varphi}\delta\varphi\mathrm{d}x. \tag{36}$$

In the integral term on the far right of this equation, $\left|\boldsymbol{\nabla}\phi_c\right|$ and $\mathbf{n}_\Gamma$ are present, hence this part of the integral term primarily governs the results of the interface region.

2.3. Numerical implementation

The algorithm scheme is illustrated in Fig. 1. We solve the coupled terms

$$F\Big|_\Omega = F_1 + F_2 + F_3 + F_4 \tag{37}$$

firstly and then solve the advection Eq. (25) and reinitialization Eq. (26) separately and sequentially. It is necessary to establish boundary conditions for both velocity and pressure. For the free-falling jet problem, boundary conditions for the level set function must also be set at the fluid inlet boundary to simulate the continuous injection of the fluid. In the case of the droplets example, there is no need to set any boundary conditions related to the level set function on the boundaries, as detailed in Section 3. The process involves two iterations, both pertaining to the same time step. In the first iteration, we solve the balance equations, and in the second iteration, we solve the advection equation based on the velocity field results. Subsequently, in the third step, which is a sub-iteration at each time step, we carry out the reinitialization process. We employ linear Lagrange elements for the interpolation of velocity, pressure, electric potential, and level set function. The standard FEM approach, characterized by piecewise continuity, guarantees a monotonous convergence. All unknown fields are simultaneously solved, yielding precise solutions in coupled terms. The shape functions are continuous on an element-by-element basis across the entire domain, exerting influence only locally due to their compact support on the element. Such representation fits the approximation in the Hilbertian Sobolev space $\mathscr{H}^1$ (Zohdi, 2018). Within each element, interpolation is of order q and encompasses $\mathscr{P}_q$ on a mesh, $\mathscr{T}$, comprised of elements, Ω^E. For both scalar and vector spaces, the first-order interpolation polynomial serves as the shape function, indicative of our usage of linear Lagrange elements for pressure and velocity,

$$\mathscr{V} = \left\{ \{\phi_c,\bar{\varphi},\bar{p},\bar{\boldsymbol{v}}\} \in \mathscr{H}^1(\Omega) : \{\phi_c,\bar{\varphi},\bar{p},\bar{\boldsymbol{v}}\}\Big|_{\Omega^\mathrm{E}} \in \mathscr{P}_1(\Omega^\mathrm{E})\ \forall\Omega^\mathrm{E}\in\mathscr{T} \right\}. \tag{38}$$

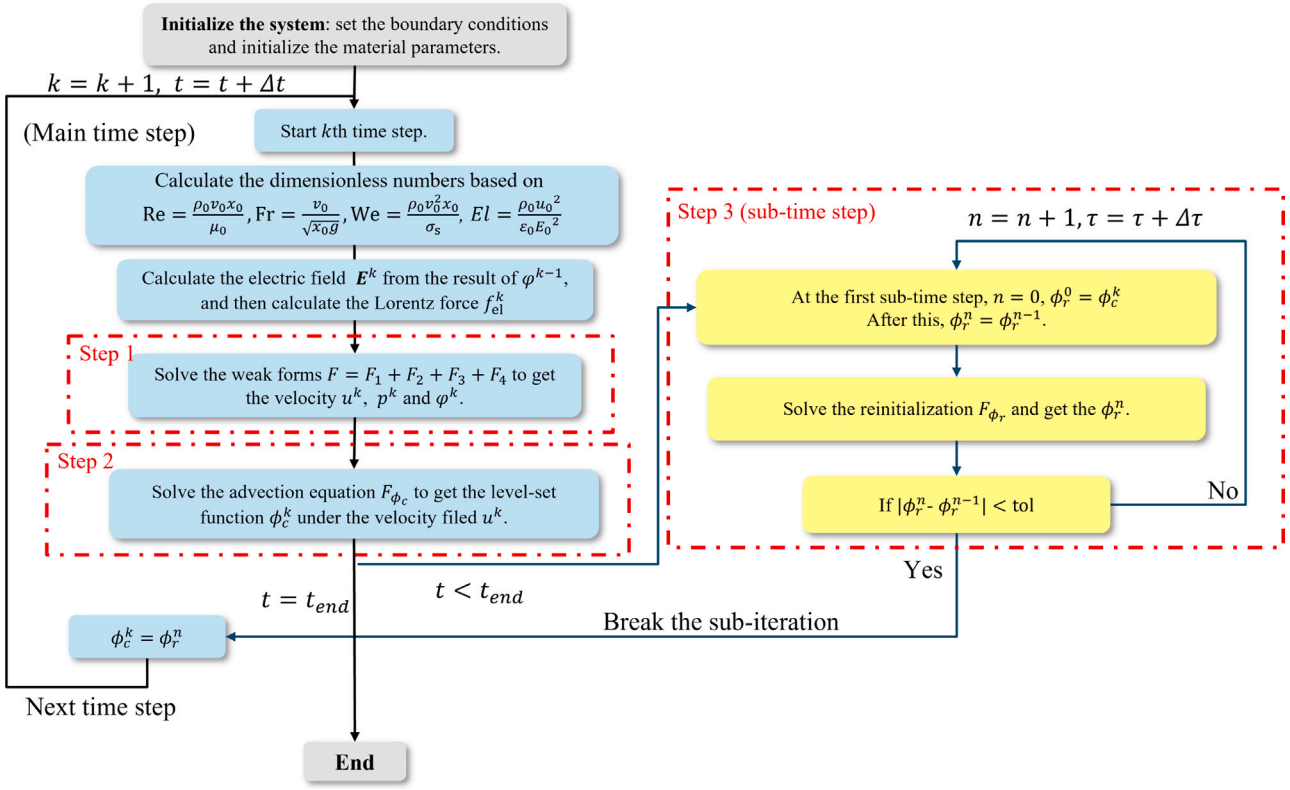

Fig. 1. The flowchart consists of blue squares that denote the processes in a time step, and yellow squares that indicate the processes of the sub-time step. (For interpretation of the references to color in this figure legend, the reader is referred to the web version of this article.)

3. Results

Herein we contemplate finite element models for two distinct problems. Initially, we investigate the coupling of a free-falling jet with an electric field, illustrating the interplay between electric fields and fluid dynamics. Additionally, we establish a finite element model that couples microdroplets with electric fields, delving into the deformation and breakup behaviors of microdroplets under the influence of the electric field. In Section 2.1, we employ the P1/P1 elements by applying an accurate finite element method and incorporating F_3 for numerical stabilization of mixed formulations. As seen in Eq. (37), we simultaneously solved the coupled terms of the fluid governing equations F_1, F_2, F_3, along with the electricity governing equation F_4. This approach significantly enhanced computational efficiency, enabling us to use finer grids for more accurate simulation of the interfaces in two-phase flows. To demonstrate the computational efficiency of this method, we compared it with results obtained using the P2/P1 elements in a projection method, which sequentially solves the fluid and electricity governing equations; this projection format is referenced in the cited article (Guermond and Quartapelle, 1997). We concurrently executed a solution for a 2D example on a triangular mesh comprising 11,830 nodes and 2325 cells. The computational platform utilized is equipped with an i5-13400F processor, 2 × 16 GB 4400 MHz DDR5 ROM. Parallel computation is conducted using 'mpirun' to engage 6 cores, with the final time consumption detailed in Table 1. The results indicate that the method adopted in this paper significantly reduces computational time. This reduction allows us to employ finer meshes, thereby rendering the transition zone at the interface sharper. It is particularly noteworthy that in the example of a free-falling jet (illustrated in Fig. 5), there are 40 elements across the inlet segment (Γ_1 in Fig. 4). In the subsequent example involving microdroplets, the diameter of a droplet is discretized into 56 elements.

Next, we use Rickert's experimental data (Rickert, 2023) of an oil droplet deforming in an electric field as a benchmark to verify our numerical implementation. We establish the corresponding numerical model as shown in Fig. 2. From Fig. 2, it is evident that we have employed two distinct fluids: silicone oil in Ω_2 (represented by the black droplet) and castor oil in Ω_1 (illustrated as the blue base). D is the size of the domain. The material parameters are presented in Table 2.

We use the parameters of silicone oil as a reference for non-dimensionalization. In addition to this, other reference data include,

Table 1
Time consumption.

Methods	Total time
An accurate FEM with P1/P1 elements	542.092 s
Projection with P2/P1 elements	1433.156 s

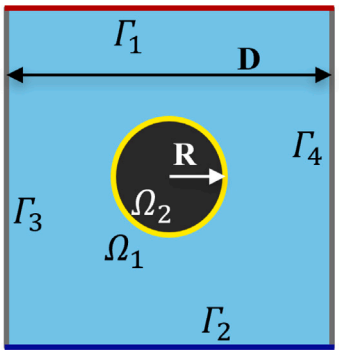

Fig. 2. The figure represents a numerical model of an oil droplet. The black portion signifies the silicone oil droplet, while the blue portion represents the castor oil base. The interface is delineated in yellow. Electrode plates are positioned above and below. (For interpretation of the references to color in this figure legend, the reader is referred to the web version of this article.)

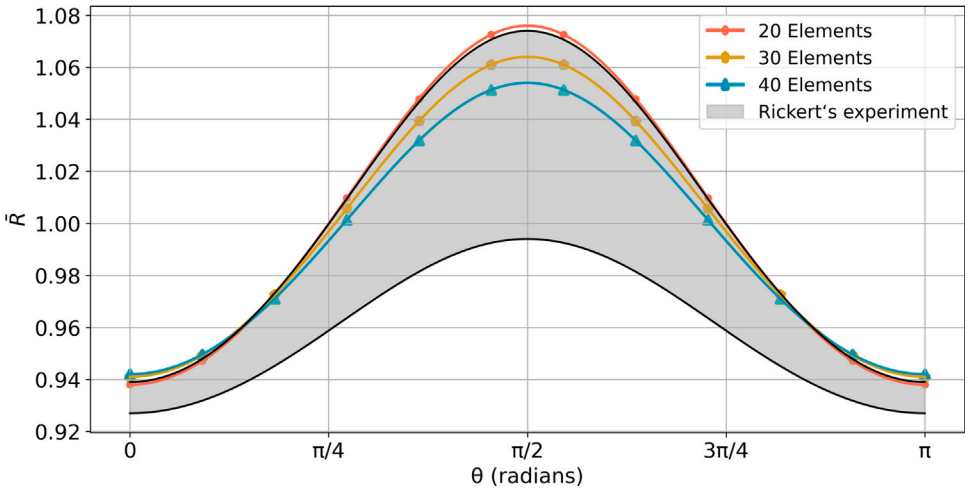

Fig. 3. The curves in the figure represent the semi-elliptical contour of the deformed droplet unfolded in a Cartesian coordinate system, where the horizontal axis represents the angle. The values of the vertical axis at the positions of 0 and π on the horizontal axis correspond to the results of the minor axis, and the value of the vertical axis at the position of $\pi/2$ on the horizontal axis corresponds to the result of the major axis.

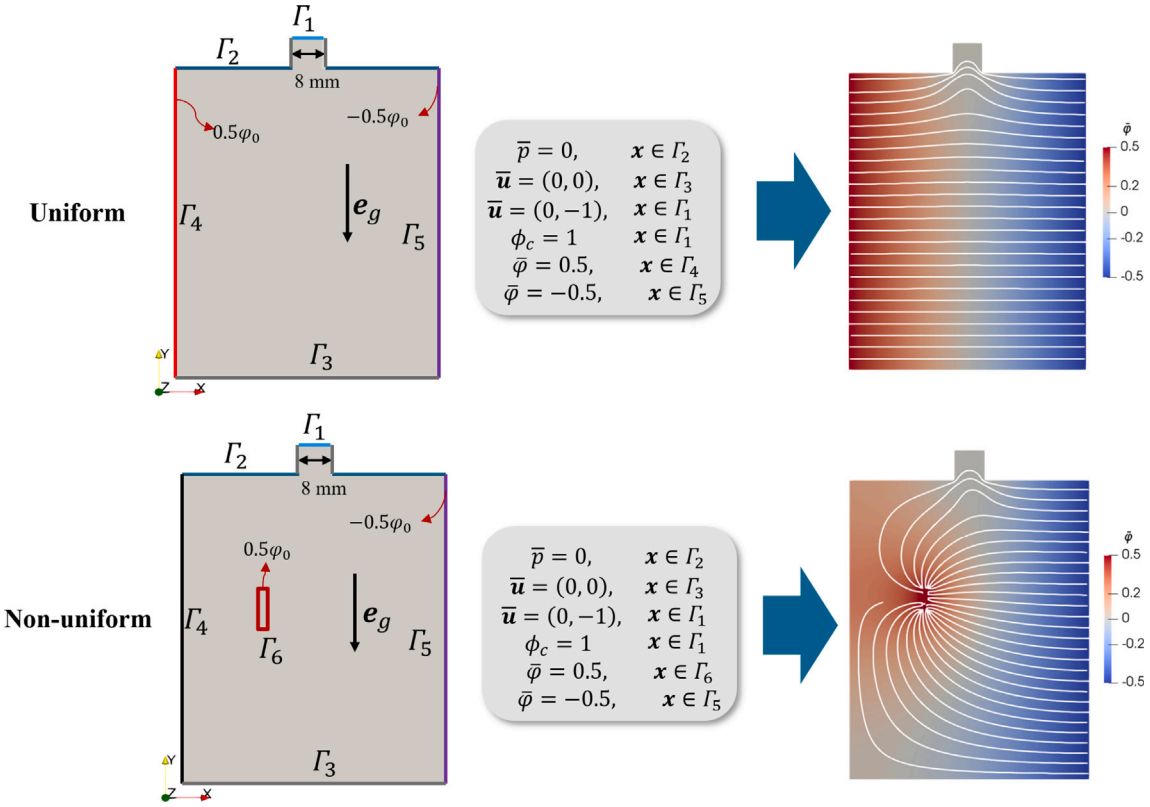

Fig. 4. The figures display the finite element models and boundary conditions for both the initially uniform and non-uniform electric fields. Left: boundary conditiont are sketched. Right: uniform and non-uniform electric field results generated from the two examples are illustrated. The background cloud map depicts the distribution of electric potential, with the electric field represented by white iso-lines.

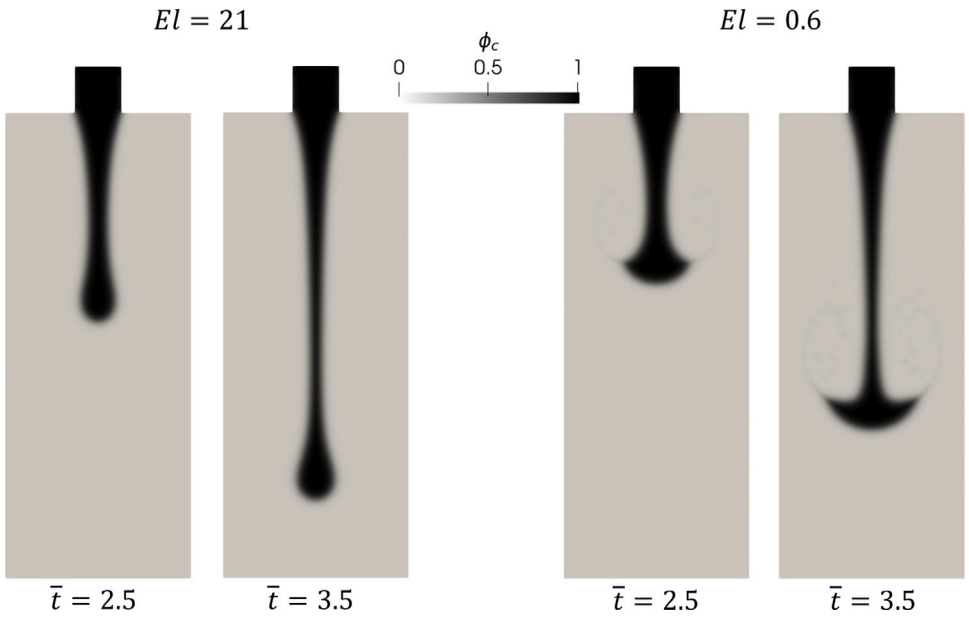

Fig. 5. Distribution of ϕ_c at $El = 21$ (left) and $El = 0.6$ (right), indicating the state of the jet flow at $\bar{t} = 2.5$ and $\bar{t} = 3.5$. The black portion represents fluid with $\phi_c = 1$, while the gray portion denotes air with $\phi_c = 0$.

Table 2
Material parameters.

Name	Symbol	Value in Ω_1	Value in Ω_2
Mass density (g/mm^3)	ρ	0.98×10^{-3}	0.98×10^{-3}
Viscosity (Pa s)	μ	6.5	5.39
Relative permittivity	ϵ^{r}	7.3	3.772

$$\ell_{\mathrm{ref}} = R = 0.6 \text{ mm}, \quad E_{\mathrm{ref}} = 495 \ \frac{\mathrm{V}}{\mathrm{mm}}, \quad \sigma_{\mathrm{ref}} = 5.5 \ \frac{\mu\mathrm{N}}{\mathrm{mm}}, \quad v_{\mathrm{ref}} = \sqrt{\frac{\sigma_1}{\rho_{\mathrm{ref}} \ell_{\mathrm{ref}}}}, \tag{39}$$

and dimensionless-related parameters are $Re = 1.06 \times 10^{-2}$, $Fr = 1.56$, $We = 1$, $El = 4.226$. The boundary conditions are as follows:

$$\bar{p} = 0, \ x \in \Gamma_3, \Gamma_4; \quad \bar{\mathbf{u}} = (0,0), \ x \in \Gamma_1, \Gamma_2; \quad \bar{\varphi} = \bar{\varphi}_0, \ x \in \Gamma_1; \quad \bar{\varphi} = -\bar{\varphi}_0, \ x \in \Gamma_2. \tag{40}$$

We used three different mesh sizes, classified by the number of elements on the droplet radius length R, which are 20, 30, and 40 elements, respectively. The dimensionless size of the domain $D = 8$ and the dimensionless radius of the droplet $\bar{R} = 1$. We choose the boundary condition $\bar{\varphi}_0 = D/2$ to ensure that the dimensionless electric field strength $\bar{E}_{\mathrm{ideal}} = 2\bar{\varphi}_0/D = 1$ under ideal conditions (assuming that the domain is homogeneous).

Fig. 3 compares the different results with the experimental results in the benchmark. The experimental results are displayed as a gray area with black curves representing the upper and lower boundaries. As the mesh is refined, the results gradually converge, and the convergence of the minor axis results is more pronounced. Compared to the experiment, the minor axis part is slightly off, and the result with 40 elements only differs by 3 ‰ from the upper boundary of the short side. In contrast, the major axis part falls within the range of experimental results. Most numerical data fall within the experimental area and show a convergence trend. The method of this paper is in good agreement with the experimental results.

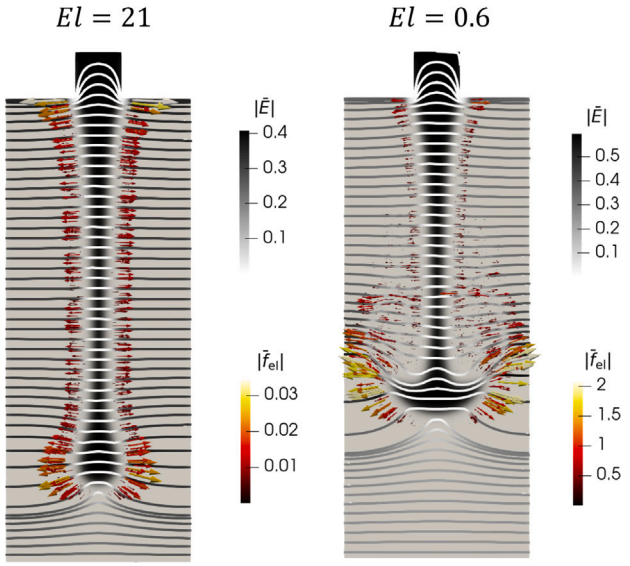

Fig. 6. Results of the electric field lines and the Lorentz force from $El = 21$ and $El = 0.6$ at $\bar{t} = 3.5$. The background represents the ϕ_c results. The electric field lines are represented in black and white to indicate the strength of the field. The Lorentz force is indicated by arrows scaled (and colored) by their magnitude. (For interpretation of the references to color in this figure legend, the reader is referred to the web version of this article.)

3.1. Free-falling jet

For the free-falling jet example, we examine the impact of both initially uniform and non-uniform electric fields on the jet path, as depicted in Fig. 4. In this problem, the two phases are represented by fluid and air. We allow the fluid to continually enter the container space from the inlet boundary, Γ_1, forming a steady jet under the influence of the inlet velocity and gravity. We model the ejection by setting velocity boundary condition, $\bar{\boldsymbol{u}}$, and level set function value boundary condition, ϕ_c, on Γ_1. A constant velocity vector $(0, -1)$ is established on this boundary, and the level set function value is consistently set to 1, facilitating the simulation of continuous flow at this boundary.

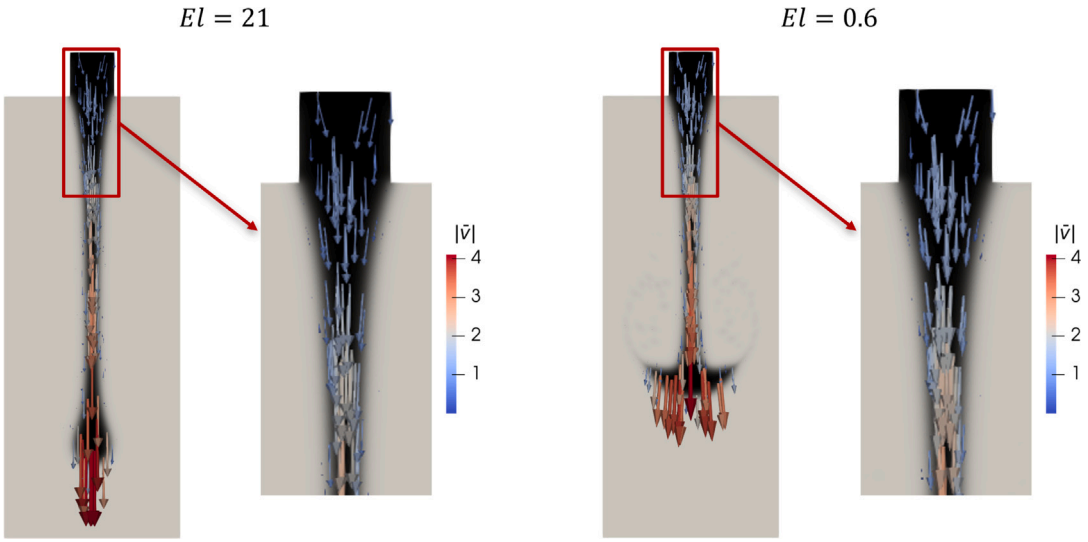

Fig. 7. Velocity distribution of the fluid, with a magnified view of the initial shrinking segment from $El = 21$ and $El = 0.6$ at $\bar{t} = 3.5$. The black and gray backgrounds represent the results for ϕ_c. The velocity results are indicated by colored arrows scaled by their magnitude. For the sake of an intuitive visualization of the velocity specifically for the fluid part, the velocity here is scaled by the function ϕ_c that suppresses the velocity distribution within the air. (For interpretation of the references to color in this figure legend, the reader is referred to the web version of this article.)

Once this flow stabilizes, a steady jet is successfully simulated. For the uniform electric field case, electrodes in the upper of Fig. 4, Γ_4 and Γ_5, are at equal length and set up at both sides of the container. For the non-uniform electric field, we reposition the left electrode plate Γ_6 to the inner of the container and significantly reduce its width. On the electrode boundaries, we set electrical potential boundary conditions to generate an electric field. For the remaining boundaries, we impose conditions of zero pressure and no-slip boundary conditions, respectively, shown in Fig. 4.

For the fluid phase, we chose a density of 0.956×10^{-3} g/mm^3, viscosity of 0.57 Pa s, surface tension coefficient of 35.9 μN/mm, and relative permittivity of 81. For air, the density is 1×10^{-6} g/mm^3, viscosity is 0.001 Pa s, and relative permittivity is 1. We stress that the choice of a relatively high viscosity coefficient for air is to circumvent issues of non-convergence in numerical computation. Even if the viscosity would be chosen correctly, we are using an incompressible flow assumption that anyways set the velocity profile of air in question. In general, we skip evaluation of the calculated air velocity in this computation. The fluid outlet width is 8 mm, and the distance between the left and right boundaries of the container is 32 mm. The reference velocity of the inlet flow is 400 mm/s. Based on these selected parameters, the resulting dimensionless numbers are $Re = 2.7, We = 8.5, Fr = 0.7$. For different choices of the reference potential difference φ_0 we consider two conditions $El = 21, El = 0.6$ and a smaller El number means a larger electric field strength.

Fig. 5 illustrates the jet flow at two distinct El numbers. We have chosen the ϕ_c results from two different time instances to depict the current status of the jet. The profound influence of a high electric field strength (small El number) on the jet is evident. As observed from the $\bar{f}_{\mathrm{el}}$ results in Fig. 6, the entire jet experiences a Lorentz force pulling it laterally in both directions and this force acts along the direction of the electric field lines. The part on jet tail seem to be most significantly impacted. This phenomenon is caused by the initial shrinking segment of the free-falling jet—as seen in the velocity results of Fig. 7—the fluid at the interface possesses a horizontal velocity component combined with a longitudinal surface tension. The nearly horizontal Lorentz force counters the fluid's inertia, and its component parallel to the interface contour is minimal. In contrast, for the jet tail, since their shape is already stabilized and velocity is mainly in the vertical direction, which lets the effect of the Lorentz force to become pronounced.

Fig. 8 demonstrates the impact of a non-uniform electric field on the jet. In contrast to the generally symmetrical results shown in Fig. 5; Fig. 8 reveals how the jet trajectory is distorted by the non-uniform electric field. From the vector representation of the electric field and the contour lines of the potential, we observe the impact of the jet as it enters the electric field on both the field distribution and potential distribution. Conversely, changes in the electric field and potential distributions also influence the path of the jet. Ultimately, we notice that the continuous jet, under the influence of this non-uniform electric field, breaks into segmented droplets, which represents a complex interaction process. This phenomenon can be explained by the non-uniform electric field.

As the results in Fig. 9, which focus on lower middle area of $\bar{t} = 6 \sim 9$ results in Fig. 8, we understand that a vertical electric field component causes a substantial Lorentz force $\bar{f}_{\mathrm{el}}$ component, which is generated on the jet interface, parallel to the interface contour. The direction of $\bar{f}_{\mathrm{el}}$ is perpendicular to the equipotential line (along the direction of the electric field), so the distribution of the equipotential line can roughly determine the direction of $\bar{f}_{\mathrm{el}}$ caused by this part. When the component of $\bar{f}_{\mathrm{el}}$ reaches a certain magnitude in the direction of surface tension, it can disrupt the continuous jet, leading to the formation of droplets.

3.2. Microdroplet

In Fig. 10, we showcase an example of a microdroplet. In this instance, we chose water and oleic acid as the two phases and investigated both the scenarios of a water droplet in oleic acid and an oleic acid droplet in water. Given that the relative permittivity of water exceeds that of oleic acid, this also illustrates the differences in the Lorentz forces generated at the interface in a two-phase flow with different dielectric constants. In Fig. 10, within the channel slightly to the left of the center, there are two parallel plate electrodes of equal length. The left and right sides of the channel serve as the inlet and outlet for the base fluid, respectively. Driven by the flow of the base fluid, the droplet moves into the electric field. For the

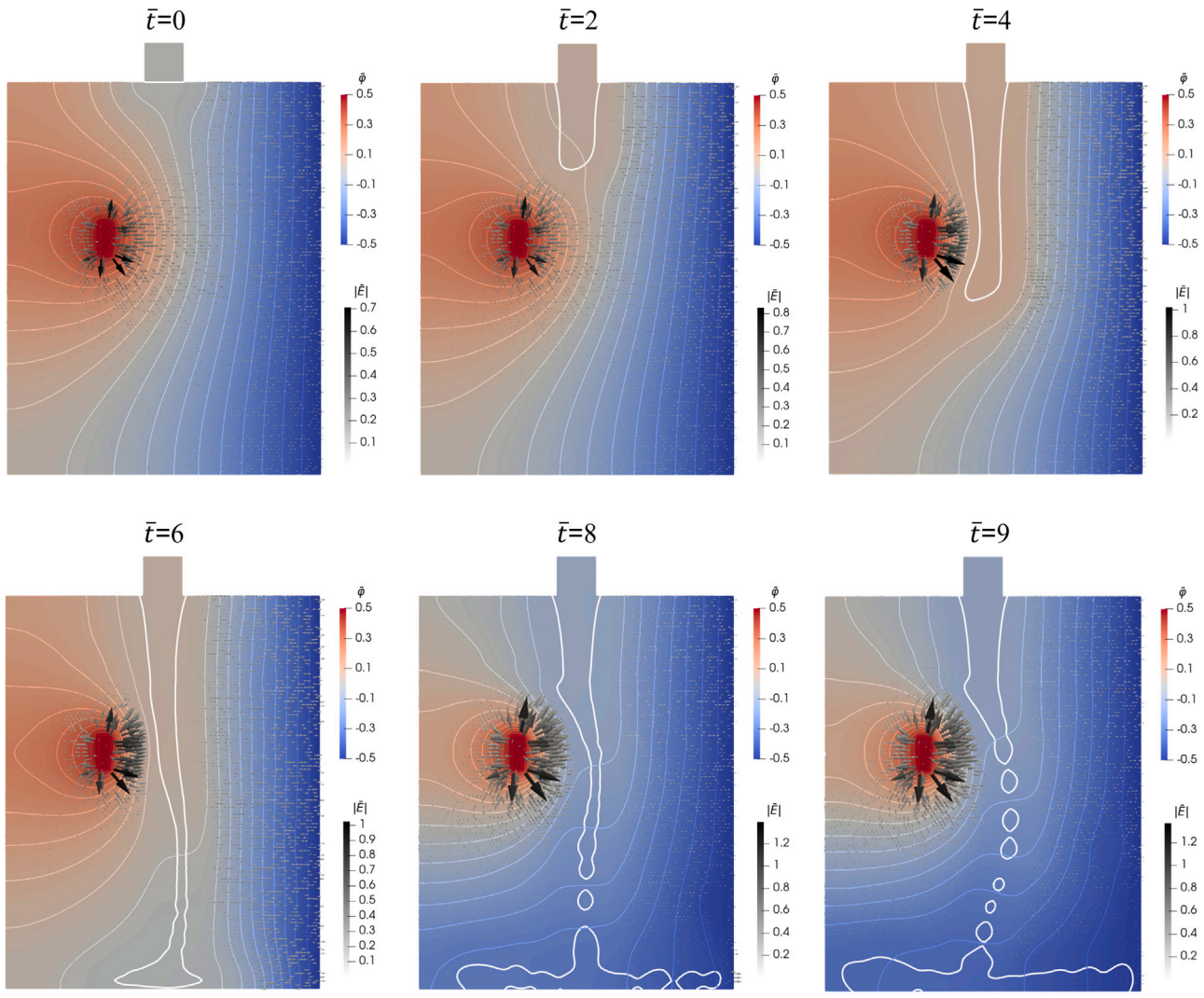

Fig. 8. The figures illustrate the interaction between the jet and the electric field in a non-uniform electric environment. The blue-red cloud background represents the electric potential results, with contour lines indicating levels of equal potential. Black and gray arrows indicate the direction of the electric field lines, with their size and shade denoting the magnitude of the field strength at that location. The highlighted white line in the figure represents the jet's contour (the interface between the jet and the air). This contour is depicted by using the result with $\phi_c = 0.5$. (For interpretation of the references to color in this figure legend, the reader is referred to the web version of this article.)

velocity boundaries on the left and right (inlet and outlet), we set non-dimensional velocity boundary conditions of $\bar{\boldsymbol{u}} = (1, 0)$. At the positions of the electrode plates on the top and bottom boundaries, non-dimensionalized electrical potential boundary conditions are established: $\bar{\varphi} = 0.5$ on the red boundary and $\bar{\varphi} = -0.5$ on the blue boundary. For the rest of the boundaries, we apply no-slip boundary conditions. It should be emphasized that gravity is neglected in this example, leading to the omission of gravity-related terms in Eqs. (22), (23), (24).

In this section, we select two specific fluids: oleic acid and water. The material parameters are presented in Table 3. The reference velocity is $v_{\text{in}} = v_{\text{out}} = 100$ mm/s and we choose the droplet's material parameters as the reference values and the dimensionless numbers are shown in Table 4.

Fig. 11 illustrates the evolution of an oleic acid droplet under varying El numbers (various electric potential differences). Initially, it is observed that due to the relative permittivity of oleic acid being lower than that of the base fluid, water, the droplet undergoes compression from the Lorentz force as it enters the electric field, and we call it a "squeezing mode". As the El number decreases, indicating an intensifying electric field strength, the droplet transitions from deformation to fission. Fig. 12 showcases the impact of altering the electrode plate length at $El = 0.317$. At this El number, a short action time of the Lorentz force induces only a deformation in the droplet. However, extending the electrode plate, which essentially prolongs the action time of the Lorentz force, leads to droplet breaking out.

Table 3
The material parameters of oleic acid and water.

Fluid	Viscosity (Pa s)	Surface tension (μN/mm)	Density (g/mm^3)	Relative permitivitty
Oleic acid	0.039	31.92	0.89×10^{-3}	3
Water	1×10^{-3}	–	1×10^{-3}	81

Table 4
The dimensionless numbers.

Droplet	Re	We	El
Oleic acid	9.128	1.115	0.317, 0.178, 0.114
Water	400	1.253	0.089, 0.060, 0.050

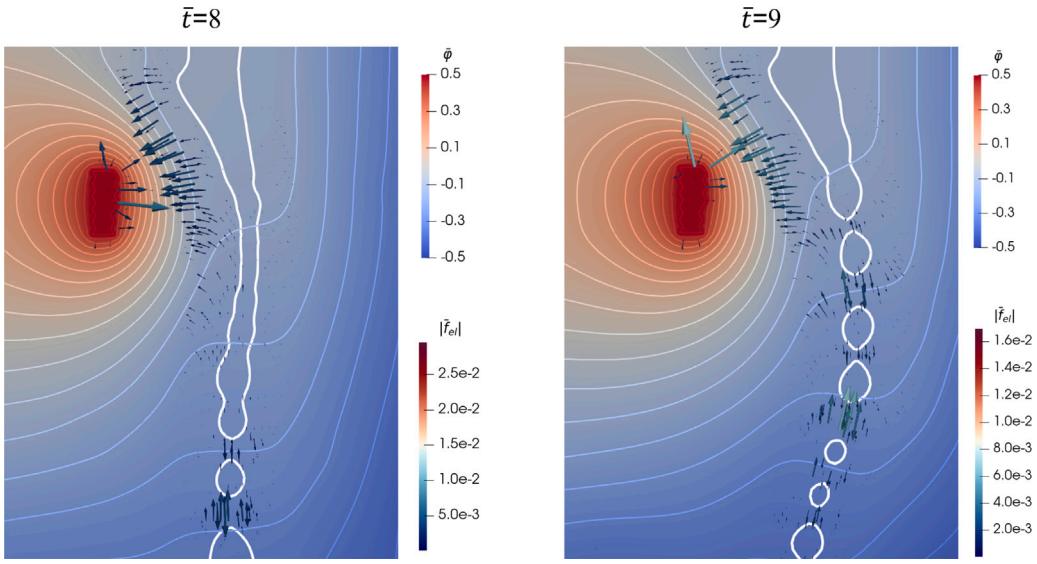

Fig. 9. The figures illustrate the results of $\bar{f}_{el}$ at certain area at $\bar{t} = 8$ and $\bar{t} = 9$ The arrows indicate the direction of the Lorentz force, with their size and color denoting the magnitude of the Lorentz force. (For interpretation of the references to color in this figure legend, the reader is referred to the web version of this article.)

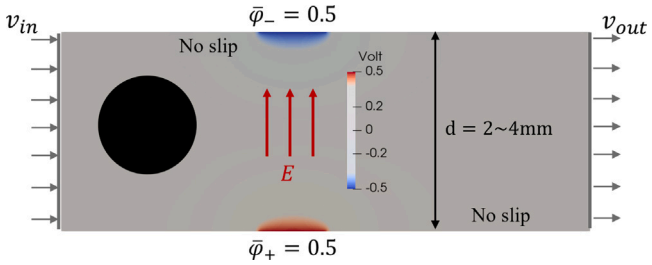

Fig. 10. The black part is the droplet, and the gray part is the base fluid. The red area is the electrode with positive potential, and the blue area is the electrode with negative potential. (For interpretation of the references to color in this figure legend, the reader is referred to the web version of this article.)

The results for water droplets are shown in Fig. 13. Contrary to the squeezing mode observed for oleic acid droplets, the water droplets exhibit a stretching mode. This is attributed to the relative permittivity of the droplet being higher than that of the base fluid in this case and this can also be explained in Eq. (36), where the different relative permittivity of the two phases lead to different signs of the rightmost integral term. Analogous to the previous case, at higher *El* numbers, only deformation of the droplet is observed. As the *El* number decreases, leading to an increase in field strength, the water droplet undergoes fragmentation, with the intensity of breakup directly proportional to the field strength.

4. Conclusion

In this study, We propose a new numerical implement for enhancing computational efficiency in such problems by combining the P1/P1 scheme with finite element simulation of multiphase flows. The effectiveness of this implement has also been validated through comparison with experimental results. We integrated Gauß's law with the level set function, generating a novel weak form of the governing equation. Utilizing the Finite Element Method, this weak form equation, together with the associated fluid dynamics equations, was solved, thus realizing numerical simulations for the coupled problem at hand.

For the free-falling jet case, the intricate mechanisms of the Lorentz force and its consequential effects were meticulously detailed, unveiling the interaction intricacies inherent to such multiphysics problems. In the context of microdroplets, emphasis was laid upon the squeezing and stretching modes. Both modes offered insights into the deformation and fragmentation behaviors of droplets under the influence of an electric field.

In essence, this research paves the way for a profound understanding and manipulation of electro-fluidic systems. We provide an open-access numerical simulation code for studying such multiphysics problems. This work can continue to be improved, for example, combined with the AMR method to further improve computational efficiency and extended to 3D models. It is foreseeable that the study of microdroplet behaviors has promising applications in therapeutic agent delivery, electrohydrodynamic atomization (EHDA), 3D-printing and ink-jet printing, among others.

CRediT authorship contribution statement

Yiming Liu: Writing – original draft, Software, Conceptualization, Data curation, Formal analysis, Investigation, Methodology. **Bilen Emek Abali:** Writing – review & editing, Supervision, Resources, Formal analysis, Conceptualization. **Wolfgang H. Müller:** Resources, Funding acquisition, Supervision, Writing – review & editing.

Declaration of competing interest

The authors declare that they have no known competing financial interests or personal relationships that could have appeared to influence the work reported in this paper.

Data availability

Github: https://github.com/liuyiming0507/FluidwithElectricField.

Acknowledgments

Author Y. L. gratefully acknowledges financial support from the China Scholarship Council, China (CSC, 202006120055).

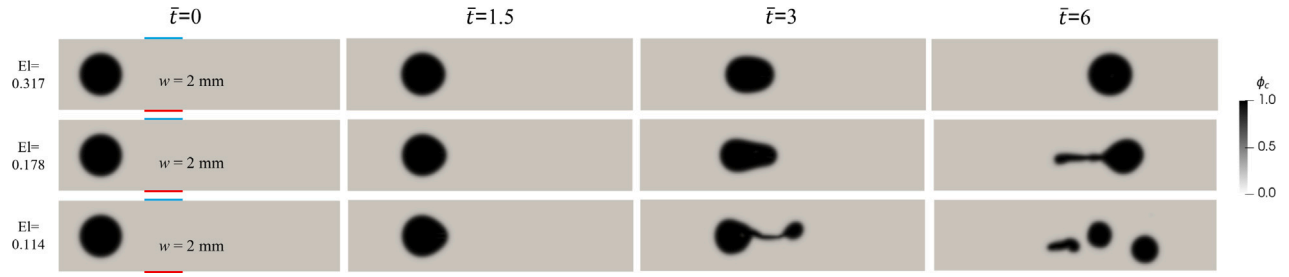

Fig. 11. The figures depict the oleic acid droplet results for ϕ_c at various computational times under different El numbers. The width of all electrode plates is $w = 2$ mm. Black and gray represent the two phases respectively.

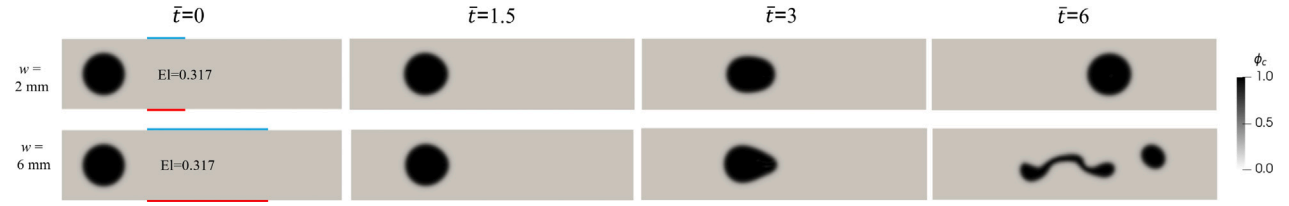

Fig. 12. The figures depict the oleic acid droplet results for ϕ_c at various computational times under different widths ($w = 2, w = 6$) of the electrode plates. The El number of all cases is 0.317.

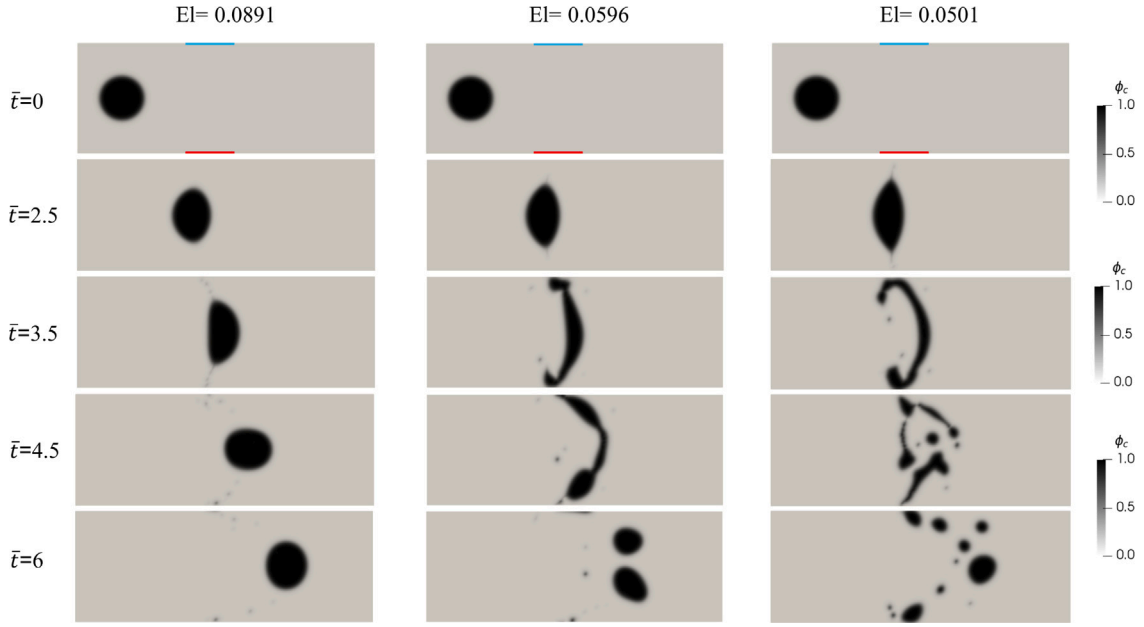

Fig. 13. The figures depict the water droplet results for ϕ_c at various computational times under different El numbers. The width of all electrode plates is $w = 2$ mm. Black and gray represent the two phases respectively.

References

Abali, B.E., 2017. Computational reality. In: Advanced Structured Materials, vol. 55, Springer Nature, Singapore.

Abali, B.E., 2019. An accurate finite element method for the numerical solution of isothermal and incompressible flow of viscous fluid. Fluids 4 (1), 5.

Abali, B.E., Queiruga, A., 2019. Theory and computation of electromagnetic fields and thermomechanical structure interaction for systems undergoing large deformations. J. Comput. Phys. 394, 200–231.

Abali, B.E., Reich, F.A., 2020. Verification of deforming polarized structure computation by using a closed-form solution. Contin. Mech. Thermodyn. 32 (3), 693–708.

Abali, B.E., Savaş, Ö., 2020. Experimental validation of computational fluid dynamics for solving isothermal and incompressible viscous fluid flow. SN Appl. Sci. 2, 1–16.

Antepara, O., Balcázar, N., Oliva, A., 2021. Tetrahedral adaptive mesh refinement for two-phase flows using conservative level-set method. Internat. J. Numer. Methods Fluids 93 (2), 481–503.

Ashour, M., Valizadeh, N., Rabczuk, T., 2021. Isogeometric analysis for a phase-field constrained optimization problem of morphological evolution of vesicles in electrical fields. Comput. Methods Appl. Mech. Engrg. 377, 113669.

Ashour, M., Valizadeh, N., Rabczuk, T., 2023. Phase-field Navier–Stokes model for vesicle doublets hydrodynamics in incompressible fluid flow. Comput. Methods Appl. Mech. Engrg. 412, 116063.

Bowman, E.K., Alper, H.S., 2020. Microdroplet-assisted screening of biomolecule production for metabolic engineering applications. Trends Biotechnol. 38 (7), 701–714.

Brackbill, J., Kothe, D., Zemach, C., 1992. A continuum method for modeling surface tension. J. Comput. Phys. 100 (2), 335–354.

Calvert, P., 2001. Inkjet printing for materials and devices. Chem. Mater. 13 (10), 3299–3305.

Campanholi, K.d.S.S., da Silva, J.B., Batistela, V.R., Gonçalves, R.S., Dos Santos, R.S., Balbinot, R.B., Lazarin-Bidóia, D., Bruschi, M.L., Nakamura, T.U., Nakamura, C.V., et al., 2022. Design and optimization of stimuli-responsive emulsion-filled gel for topical delivery of copaiba oil-resin. J. Pharm. Sci. 111 (2), 287–292.

Cardiff, P., Demirdžić, I., 2021. Thirty years of the finite volume method for solid mechanics. Arch. Comput. Methods Eng. 1–60.
Chaudhuri, J., Timung, S., Dandamudi, C.B., Mandal, T.K., Bandyopadhyay, D., 2017. Discrete electric field mediated droplet splitting in microchannels: Fission, cascade, and Rayleigh modes. Electrophoresis 38 (2), 278–286.
Chen, X., Ware, H.O.T., Baker, E., Chu, W., Hu, J., Sun, C., 2017. The development of an all-polymer-based piezoelectric photocurable resin for additive manufacturing. Procedia CIRP 65, 157–162.
Fan, J., Deneke, N., Xu, S., Newell, B., Garcia, J., Davis, C., Wu, W., Voyles, R.M., Nawrocki, R.A., 2022. Electric poling-assisted additive manufacturing technique for piezoelectric active poly (vinylidene fluoride) films: Towards fully three-dimensional printed functional materials. Addit. Manuf. 60, 103248.
Fernández-Gutiérrez, D., Zohdi, T.I., 2020. Delta voronoi smoothed particle hydrodynamics, δ-VSPH. J. Comput. Phys. 401, 109000.
Ferziger, J.H., Perić, M., Street, R.L., 2019. Computational Methods for Fluid Dynamics. springer.
Firouznia, M., Bryngelson, S.H., Saintillan, D., 2023. A spectral boundary integral method for simulating electrohydrodynamic flows in viscous drops. J. Comput. Phys. 489, 112248.
Giannitelli, S.M., Limiti, E., Mozetic, P., Pinelli, F., Han, X., Abbruzzese, F., Basoli, F., Del Rio, D., Scialla, S., Rossi, F., et al., 2022. Droplet-based microfluidic synthesis of nanogels for controlled drug delivery: tailoring nanomaterial properties via pneumatically actuated flow-focusing junction. Nanoscale 14 (31), 11415–11428.
GNU Operating System, 2007. GNU general public license. http://www.gnu.org/copyleft/gpl.html.
Guermond, J.-L., Quartapelle, L., 1997. Calculation of incompressible viscous flows by an unconditionally stable projection FEM. J. Comput. Phys. 132 (1), 12–33.
Hansen, K.B., Arzani, A., Shadden, S.C., 2019. Finite element modeling of near-wall mass transport in cardiovascular flows. Int. J. Numer. Methods Biomed. Eng. 35 (1), e3148.
Hashemi, M.R., Ryzhakov, P.B., Rossi, R., 2020. An enriched finite element/level-set method for simulating two-phase incompressible fluid flows with surface tension. Comput. Methods Appl. Mech. Engrg. 370, 113277.
Hirt, C.W., Nichols, B.D., 1981. Volume of fluid (VOF) method for the dynamics of free boundaries. J. Comput. Phys. 39 (1), 201–225.
Jeong, J., Chung, S., Lee, J.-B., Kim, D., 2021. Electric field-driven liquid metal droplet generation and direction manipulation. Micromachines 12 (9), 1131.
Jia, T.Z., Chandru, K., 2023. Recent progress in primitive polyester synthesis and membraneless microdroplet assembly. Biophys. Physicobiol. 20 (1), e200012.
John, V., et al., 2016. Finite Element Methods for Incompressible Flow Problems, vol. 51, Springer.
Kamali, R., Manshadi, M.K.D., 2016. Numerical simulation of the leaky dielectric microdroplet generation in electric fields. Internat. J. Modern Phys. C 27 (01), 1650012.
Lafaurie, B., Nardone, C., Scardovelli, R., Zaleski, S., Zanetti, G., 1994. Modelling merging and fragmentation in multiphase flows with SURFER. J. Comput. Phys. 113 (1), 134–147.
Lee, C., Tarbutton, J.A., 2014. Electric poling-assisted additive manufacturing process for PVDF polymer-based piezoelectric device applications. Smart Mater. Struct. 23 (9), 095044.
Li, Q., Zhu, H., Lu, S., Lei, M., Xu, W., Liu, Z., 2023. Numerical investigation on formation mechanism and flow law of droplet in T-junction by electric field. Phys. Fluids 35 (6).
Ling, K., Zhang, S., Wu, P.-Z., Yang, S.-Y., Tao, W.-Q., 2019. A coupled volume-of-fluid and level-set method (VOSET) for capturing interface of two-phase flows in arbitrary polygon grid. Int. J. Heat Mass Transfer 143, 118565.
Liu, C., Li, B., Liu, Q., Hong, J., Li, K., 2023. A novel implicit meshless particle method: NURBS-based particle hydrodynamics (NBPH). Comput. Methods Appl. Mech. Engrg. 406, 115895.
Liu, Y., Shu, C., Zhang, H., Yang, L., Lee, C., 2021. An efficient high-order least square-based finite difference-finite volume method for solution of compressible Navier-Stokes equations on unstructured grids. Comput. & Fluids 222, 104926.
López-Herrera, J., 2011. A charge-conservative approach for simulating electrohydrodynamic two-phase flows using volume-of-fluid. J. Comput. Phys. 230 (5), 1939–1955.
Martínez-Ferrer, P.J., Qian, L., Ma, Z., Causon, D.M., Mingham, C.G., 2018. An efficient finite-volume method to study the interaction of two-phase fluid flows with elastic structures. J. Fluids Struct. 83, 54–71.
Mehta, P., Haj-Ahmad, R., Rasekh, M., Arshad, M.S., Smith, A., van der Merwe, S.M., Li, X., Chang, M.-W., Ahmad, Z., 2017. Pharmaceutical and biomaterial engineering via electrohydrodynamic atomization technologies. Drug Discov. today 22 (1), 157–165.
Müller, I., Müller, W.H., Electrodynamics and rational thermodynamics. ZAMM-J. Appl. Math. Mech. (Z. Angew. Math. Mech.) e202300209.
Narváez-Muñoz, C., Hashemi, M.R., Ryzhakov, P.B., Pons-Prats, J., 2023. An enriched finite element/level-set model for two-phase electrohydrodynamic simulations. Phys. Fluids 35 (1).
Noh, W.F., Woodward, P., 1976. SLIC (simple line interface calculation). In: Proceedings of the Fifth International Conference on Numerical Methods in Fluid Dynamics June 28–July 2, 1976 Twente University, Enschede. Springer, pp. 330–340.
Olsson, E., Kreiss, G., 2005. A conservative level set method for two phase flow. J. Comput. Phys. 210 (1), 225–246.
Olsson, E., Kreiss, G., Zahedi, S., 2007. A conservative level set method for two phase flow II. J. Comput. Phys. 225 (1), 785–807.
Osher, S., Fedkiw, R., Piechor, K., 2004. Level set methods and dynamic implicit surfaces. Appl. Mech. Rev. 57 (3), B15.
Palzhanov, Y., Zhiliakov, A., Quaini, A., Olshanskii, M., 2021. A decoupled, stable, and linear FEM for a phase-field model of variable density two-phase incompressible surface flow. Comput. Methods Appl. Mech. Engrg. 387, 114167.
Park, C.Y., Zohdi, T.I., 2020. Semi-implicit operator splitting for the simulation of Herschel–Bulkley flows with smoothed particle hydrodynamics. Comput. Part. Mech. 7, 699–704.
Reich, F.A., Rickert, W., Müller, W.H., 2018. An investigation into electromagnetic force models: differences in global and local effects demonstrated by selected problems. Contin. Mech. Thermodyn. 30, 233–266.
Rickert, W., 2023. An Investigation of the Electromagnetic Coupling Problem by Means of a Rational Framework and Selected Experiments (Ph.D. thesis). Technische Universität Berlin.
Ristenpart, W., Bird, J., Belmonte, A., Dollar, F., Stone, H.A., 2009. Non-coalescence of oppositely charged drops. Nature 461 (7262), 377–380.
Scardovelli, R., Zaleski, S., 1999. Direct numerical simulation of free-surface and interfacial flow. Annu. Rev. Fluid Mech. 31 (1), 567–603.
Sethian, J.A., 1999. Level set methods and fast marching methods: Evolving interfaces in computational geometry, fluid mechanics, computer vision, and materials science, vol. 3, Cambridge University Press.
Shen, M., Li, B.Q., Yang, Q., 2023. A 3-D phase field study of dielectric droplet impact under a horizontal electric field. Int. J. Multiph. Flow 162, 104385.
Sohrabi, S., Moraveji, M.K., et al., 2020. Droplet microfluidics: Fundamentals and its advanced applications. RSC Adv. 10 (46), 27560.
Sussman, M., Smereka, P., Osher, S., 1994. A level set approach for computing solutions to incompressible two-phase flow. J. Comput. Phys. 114 (1), 146–159.
Tian, H., Shao, J., Ding, Y., Li, X., Liu, H., 2014. Simulation of polymer rheology in an electrically induced micro-or nano-structuring process based on electrohydrodynamics and conservative level set method. RSC Adv. 4 (42), 21672–21680.
Tian, Y., Wang, H., Zhou, X., Xie, Z., Zhu, X., Chen, R., Ding, Y., Liao, Q., 2022. How does the electric field make a droplet exhibit the ejection and rebound behaviour on a superhydrophobic surface? J. Fluid Mech. 941, A18.
Unverdi, S.O., Tryggvason, G., 1992. A front-tracking method for viscous, incompressible, multi-fluid flows. J. Comput. Phys. 100 (1), 25–37.
Villanueva, W., Amberg, G., 2006. Some generic capillary-driven flows. Int. J. Multiph. Flow 32 (9), 1072–1086.
Wang, A., Abdulla, A., Ding, X., 2019. Microdroplets-on-chip: a review. Proc. Inst. Mech. Eng. H 233 (7), 683–694.
Wang, Z.J., Fidkowski, K., Abgrall, R., Bassi, F., Caraeni, D., Cary, A., Deconinck, H., Hartmann, R., Hillewaert, K., Huynh, H.T., et al., 2013. High-order CFD methods: current status and perspective. Internat. J. Numer. Methods Fluids 72 (8), 811–845.
Wang, Q., Wang, Z., Yang, S., Li, B., Xu, H., Yu, K., Wang, J., 2021a. Experimental study on electrohydrodynamic atomization (EHDA) in stable cone-jet with middle viscous and low conductive liquid. Exp. Therm Fluid Sci. 121, 110260.
Wang, S., Ye, J., Yang, Y., 2021b. Quantitative measurement of two-phase flow by electrical capacitance tomography based on 3D coupling field simulation. IEEE Sens. J. 21 (18), 20136–20144.
Worster, G., Moffatt, K., Batchelor, G., 2000. Perspectives in Fluid Dynamics: A Collective Introduction to Current Research. Cambridge university press Cambridge, England.
Xu, J.-J., Shi, W., Hu, W.-F., Huang, J.-J., 2020. A level-set immersed interface method for simulating the electrohydrodynamics. J. Comput. Phys. 400, 108956.
Yang, Q., Li, B.Q., Ding, Y., 2013. 3D phase field modeling of electrohydrodynamic multiphase flows. Int. J. Multiph. Flow 57, 1–9.
Yu, Y., Zhu, Y., Zhang, C., Haidn, O.J., Hu, X., 2023. Level-set based pre-processing techniques for particle methods. Comput. Phys. Comm. 289, 108744.
Zagnoni, M., Le Lain, G., Cooper, J.M., 2010. Electrocoalescence mechanisms of microdroplets using localized electric fields in microfluidic channels. Langmuir 26 (18), 14443–14449.
Zhai, C., Hong, Y., Lin, Z., Chen, Y., Wang, H., Guo, T., Hu, C., 2023. An optical tweezer-based microdroplet imaging technology. Nanotechnol. Precis. Eng. (NPE) 6 (3).
Zhang, C., Zhu, Y., Hu, X., 2022. A multi-resolution SPH framework: Application to multi-phase fluid-structure interactions. arXiv preprint arXiv:2205.00707.
Zohdi, T.I., 2018. Finite Element Primer for Beginners. Springer.